CHEMICAL ENGINEERING RESEARCH AND DESIGN 120 (2017) 159–170

Contents lists available at ScienceDirect

Chemical Engineering Research and Design

journal homepage: www.elsevier.com/locate/cherd

Experimental characterization of axial dispersion in coiled flow inverters

Damiano Rossi, Luigi Gargiulo, Gleb Valitov,
*Asterios Gavriilidis, Luca Mazzei**

University College London, Department of Chemical Engineering, Torrington Place, London WC1E 7JE, UK

ARTICLE INFO

Article history:
Received 14 September 2016
Received in revised form 10 February 2017
Accepted 14 February 2017
Available online 22 February 2017

Keywords:
Coiled flow inverters
Helically coiled tubes
Axial dispersion
Residence time distribution
Microfluidics

ABSTRACT

Narrow residence time distributions (RTDs) are desirable in many chemical engineering processes. However, when a system operates in the laminar flow regime, significant fluid dynamic dispersion takes place. This problem is often encountered in micro and millifluidic devices. Exploiting the beneficial effects of secondary flow and chaotic advection, so-called coiled flow inverters (CFIs) are a promising solution for the reduction of fluid dynamic dispersion. These devices, however, have not been extensively used due to the lack of experimental data and of correlations relating the design parameters and operating conditions to the amount of axial dispersion. In this work, we investigated RTDs in micro and millifluidic devices using step input injection and UV–vis inline spectroscopy for the detection of the concentration of a tracer. Experiments were performed for different operating conditions and geometries. Helically coiled tubes (HCTs) were similarly characterized. Dispersion data were expressed in terms of an axial dispersion coefficient and an empirical correlation was derived. The experimental results show that lower axial dispersion is achieved in CFIs as compared to HCTs and straight tubes.

1. Introduction

In micro and millifluidic devices, the flow behavior is dictated by viscous forces rather than inertial forces, as a result of low operating Reynolds numbers (Squires and Quake, 2005). In devices with simple geometry (such as straight channels), the absence of turbulence makes diffusion the only transport mechanism in the radial direction and, despite the short length scales characterizing the flow, in general this is a rather slow process. A whole branch of microfluidics has been dedicated to the development of complex microstructures capable of achieving faster and effective mixing. Parallel and serial lamination, split and recombination, and flow focusing are examples of passive micromixers designed to shorten mixing times (Hessel et al., 2005; Nguyen and Wu, 2005). These are effective tools in applications in which fast mixing between different streams is required. However, in many continuous processes what is essential is attaining low fluid dynamic axial dispersion. Approaching plug-flow behavior is required for a wide range of chemical reactions as well as for the synthesis of nano and microparticles (Marre and Jensen, 2010).

A solution proposed for approaching plug-flow behavior resorts to multiphase segmented flow (Taylor, 1961). Slugs or droplets behave as small batch reactors traveling through the system, effectively reducing residence time dispersion. However, forming stable slugs or droplets, particularly for cases in which long residence times are needed, can be quite challenging. Furthermore, the introduction of an additional phase requires downstream separation, which may be undesirable in industrial applications.

In this work, we focus on a class of simple structures that have been shown to act positively on the fluid dynamics of tubular systems operating under laminar flow conditions. Exploiting the action of the centrifugal force, one can form a secondary flow that induces recirculation in the radial direction and which alters the radial velocity profile, rendering it more uniform. This flow can be achieved in helically coiled tubes, constructed with capillaries wrapped on cylindrical supports. By

---

* *Corresponding author.*
E-mail addresses: l.mazzei@ucl.ac.uk, luca.mazzei.a@gmail.com (L. Mazzei).

http://dx.doi.org/10.1016/j.cherd.2017.02.011

changing the direction of action of the centrifugal force, the radial vortices, generated by the latter, rotate around the axis of the tube; this results in further mitigation of the radial velocity gradients. This idea was firstly proposed by Saxena and Nigam (1984) in their pioneering work on coiled flow inverters (CFIs) and, since then, several works have been published in this field.

Enhanced mixing owing to secondary flow has been exploited primarily in heat transfer operations. Radial mixing induces forced convection, reducing the thickness of boundary layers and improving overall heat exchange. This, combined with the compactness of CFIs and their low manufacturing cost, has motivated several research groups to investigate the extent by which heat transfer is enhanced in these devices. Correlations between Nusselt number and design parameters of CFIs (and other systems with coiled geometries) have been widely explored theoretically (Acharya et al., 2001, 1992; Kumar and Nigam, 2005; Lemenand and Peerhossaini, 2002) and experimentally (Acharya et al., 1992; Chagny et al., 2000; Mokrani et al., 1997; Singh et al., 2014). Recently, it has become common to use the heat transfer correlation of Mandal et al. (2010), derived for CFIs. Furthermore, heat transfer in coiled configurations without flow inversion has also been widely investigated; the summary of the finding can be found in the papers of Kumar and Nigam (2007), for laminar flow, and Mridha and Nigam (2008), for turbulent flow.

In terms of industrial implementation, a review by Vashisth et al. (2008) has outlined the potential application of curved tubes; this remains the most comprehensive review on the topic. However, at the point of writing the review, only limited research had been done on topics other than heat transfer. In the last decade, the focus has started to shift to other applications. CFIs have been used as a platform for polymerization (Parida et al., 2014a,b; Mandal et al., 2011), in which case it was shown, both numerically and experimentally, that monomer conversion in coiled flow reactors was higher than that achieved in equivalent straight channel reactors. In another application, CFI membrane modules were shown to be beneficial in oxygenation and carbonation of water, with significant mass transfer enhancement being observed (Singh et al., 2016). In biotechnology, CFIs have been utilized for protein and antibody synthesis (Sharma et al., 2016; Kateja et al., 2016; Klutz et al., 2016) owing to their ability to enhance mixing and narrow down RTD widths.

Two-phase flow in CFIs deserves a separate mention due to abundance of research in this area. Fundamental studies into pressure drop (Vashisth and Nigam, 2007), gas–liquid mixing (Vashisth and Nigam, 2008a) and RTDs of a single phase in a two-phase flow (Vashisth and Nigam, 2008b) have been performed. Furthermore, slug flow in CFIs was used in continuous flow liquid–liquid extraction processes (Kurt et al., 2016; Vural Gürsel et al., 2016; Zhang et al., 2017). In this application, up to 20% increase in extraction efficiency was reported and this was explained by enhancement of mass transfer induced by the formation of Dean vortices (Kurt et al., 2016). Also, a cooling crystallization application of the CFI concept was recently reported (Hohmann et al., 2016) where narrow RTDs and smooth axial temperature profiles were outlined as the main benefits.

A general guideline for design of CFIs has being outlined by Klutz et al. (2015). In this publication, the key design parameters and the effect of each parameter on the device performance are outlined. Furthermore, the "best performance" design space of a CFI reactor is identified for the configuration and operating conditions considered. However, no general correlation for the relationship between the design variables and axial dispersion coefficients was derived. Other studies investigated the effect of number of bends (Castelain et al., 1997) and tube curvature ratio (Palazoglu and Sandeep, 2004) on RTDs, but no correlation which can be used to predict RTDs was suggested. A recent paper by Sharma et al. (2017) has proposed an empirical relation for the Peclet number as a function of the Dean number and of the number of bends. The proposed relation is only valid for a small number of bends (up to 3), which is suitable exclusively for previous design by the same authors, US. Pat. US007337835B2 (Nigam, 2008). The design consists of several 3-bend CFIs in series which can be stacked to achieve the required residence time, internal volume, heat exchange area etc. The correlation, as one would expect, cannot be used with other system configurations.

There is currently a "barrier of entry" into research on applications on CFIs. Lack of design correlations significantly limits the scope of design in several cases. The aim of this paper is to characterize experimentally the axial dispersion in coiled flow inverters considering in particular the effect of the Dean number and of the coil-to-tube diameter ratio. The latter is a crucial design parameter; however, in the literature few studies have been devoted to its effect on axial dispersion. The paper also aims to propose a correlation which can be later on utilized as a short-cut method for the design of CFIs of similar configuration to the one investigated. To this end, we resorted to a reliable and flexible experimental procedure to perform RTD experiments on different micro and millifluidic devices. The adoption of a suitable flow model was necessary to analyze and quantify fluid dynamic dispersion. The axial dispersion model (ADM) (Aris, 1960; Danckwerts, 1953; Levenspiel and Smith, 1957; Taylor, 1953) is the most adopted model; nevertheless, analytical correlations are only available for a limited class of systems, which does not include coiled flow inverters. The adoption of this model to CFIs, therefore, is also assessed.

This paper is organized as follows. In Section 2, we discuss the axial dispersion model and how to use RTDs to derive information on axial dispersion. In Section 3, we present our experimental system for performing RTD studies. In Section 4, we report the experimental results of our study on CFIs and helically coiled tubes (HCTs) and propose a correlation relating the dispersion number to the coil-to-tube diameter ratio and the Reynolds number for a fixed number of bends.

2. Theory

2.1. Axial dispersion model

The ADM is an extension of the PFR model that accounts for the longitudinal dispersion of a tracer flowing in the axial direction in straight tubes. The tracer concentration is assumed to be radially uniform (Schaschke, 2014). The model is based on the following equation:

$$\frac{\partial C}{\partial t} = -u\frac{\partial C}{\partial z} + D_{ax}\frac{\partial^2 C}{\partial z^2} \tag{2.1}$$

where C is the tracer concentration, dependent on the time t and on the axial coordinate z, u is the mean axial fluid velocity and D_{ax} is the axial dispersion coefficient, assumed to be constant. The axial dispersion coefficient is assumed to be independent of both the axial position and the tracer concentration. It relates to the axial dispersion rate in the vessel. To characterize the axial dispersion process under different conditions, one usually adopts dimensionless numbers. In dimensionless form, Eq. (2.1) reads:

$$\frac{\partial \bar{C}}{\partial \tau} = -\frac{\partial \bar{C}}{\partial \xi} + \frac{1}{Pe_L}\frac{\partial^2 \bar{C}}{\partial \xi^2} \tag{2.2}$$

where $\tau \equiv tu/L$ and $\xi \equiv z/L$, L being the length of the vessel. $\bar{C}$ denotes the dimensionless tracer concentration (the scaling factor can be chosen arbitrarily, as the equation is linear in the concentration; usually it is chosen to be equal to the inlet concentration). The model features a single parameter known as the Peclet number, $Pe_L \equiv uL/D_{ax}$.

The inverse of Pe_L is the vessel dispersion number N_L. This is a measure of the spread of tracer in the whole vessel; more precisely:

$$\frac{\delta}{L} \sim \sqrt{N_L} \tag{2.3}$$

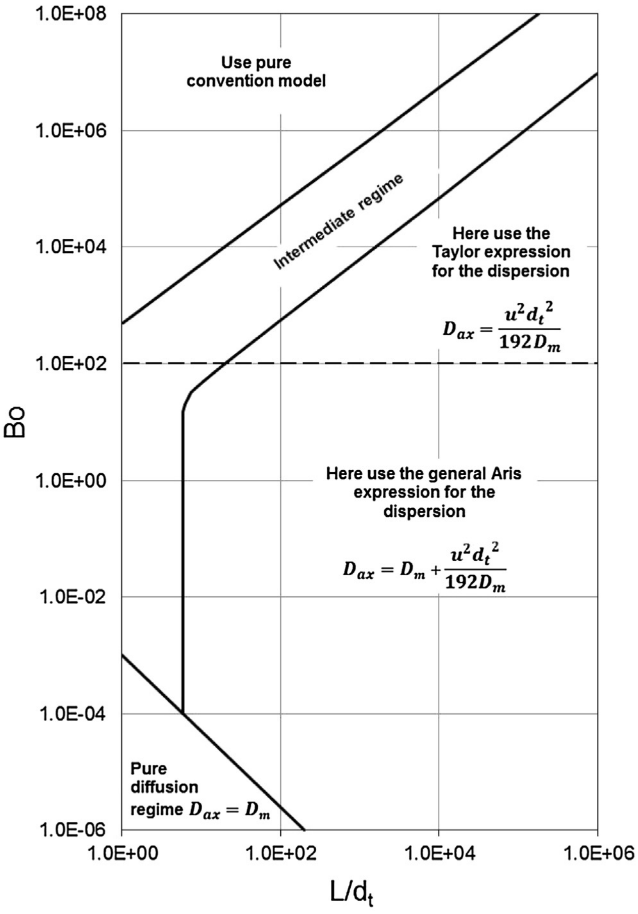

Fig. 1 – Map reporting which flow model to adopt for straight pipes. The operational point can be found on the map knowing the values of the aspect ratio of the pipe and of the Bodenstein number.
Figure recreated from Ananthakrishnan et al. (1965).

where δ is the axial spread attained at the outlet of the vessel (that is, after a time equal to L/u). Equivalently, N_L can be regarded as the ratio of the convection time to the dispersion time; thus, the larger the vessel dispersion number is, the broader the RTD is. N_L is widely used to characterize fluid dynamic dispersion and to compare dispersion performances of vessels of different lengths or operated in different fluid dynamic conditions.

Often, a similar group is employed in the literature, defined by using the pipe diameter d_t as characteristic length:

$$N_d \equiv \frac{D_{ax}}{u d_t} \tag{2.4}$$

N_d has been widely used to characterize dispersion in dimensionless flow regime maps as a function of the Reynolds number Re (Levenspiel, 1999).

The axial dispersion model can be applied to both turbulent and laminar flows. However, while in the first case there are no limitations to its applicability, for laminar flows the model holds only under certain conditions. These are reported in Fig. 1, where the system is characterized in terms of the Bodenstein number:

$$Bo \equiv Re \quad Sc \equiv \frac{\rho u d_t}{\mu} \frac{\mu}{\rho D_m} = \frac{u d_t}{D_m} \tag{2.5}$$

(D_m is the molecular diffusivity of the tracer) and of the ratio L/d_t. If the point identified by these two coordinates falls within the region of validity of the axial dispersion model, the latter is applicable. The figure also reports the analytical expressions (derived theoretically by Aris (1960) and Taylor (1953) for straight channels) needed to calculate the axial dispersion coefficient. In particular, it is:

$$Bo < 100: \quad D_{ax} = D_m + \frac{u^2 d_t^2}{192 D_m} \tag{2.6}$$

and

$$Bo > 100: \quad D_{ax} = \frac{u^2 d_t^2}{192 D_m} \tag{2.7}$$

These theoretical expressions can be verified experimentally, as described in the following section, by resorting to RTD experiments.

2.2. *Calculation of the axial dispersion coefficient*

The axial dispersion coefficient cannot be measured directly from experiments; however, it is possible to fit experimental data to the solution of the axial dispersion model (that is, of Eq. (2.1)). Two different methods of fitting experimental data exist based on the extent of axial dispersion in the system, small ($N_L < 0.01$)and large ($N_L > 0.01$).

For small extents of dispersion, the shape of the RTD curve varies little on passing through the outlet of the vessel (and in particular through the tracer detection system). This means that the resultant experimental RTD curve is close to a Gaussian distribution. In this case, the experimental RTD curve can be fitted with the analytical solution valid for open–open boundary conditions, as suggested by Levenspiel (1999):

$$N_L < 0.01: \quad E_{t,ADM} = \sqrt{\frac{u^3}{4\pi D_{ax} L}} \exp\left[-\frac{(L-ut)^2}{4 D_{ax} L}\right] \tag{2.8}$$

For large extents of dispersion, the RTD curve changes substantially on passing through the vessel outlet, becoming skewed and therefore asymmetrical. In this case, it is fitted to the following curve (Schaschke, 2014):

$$N_L > 0.01: \quad E_{t,ADM} = \frac{u}{\sqrt{4\pi D_{ax} t}} \exp\left[-\frac{(L-ut)^2}{4 D_{ax} t}\right] \tag{2.9}$$

The experimental RTD curves are fitted to Eq. (2.8) or Eq. (2.9) so that the only unknown parameter, D_{ax}, can be calculated.

This study focuses on CFIs and HCTs, not on straight pipes; therefore, there is no guarantee that the axial dispersion model (that is, Eqs. (2.8) and (2.9)) should hold and that an axial dispersion coefficient can be used to quantify the axial dispersion in these systems. This needs to be verified.

The analytical solution (either Eq. (2.8) or Eq. (2.9)) to use depends on the vessel dispersion number N_L, which is unknown before performing the fitting. As a consequence, the fitting was carried out using both solutions and then selecting the correct one. The fitting was based on the least squares method and the residual error ε of the solution was used to

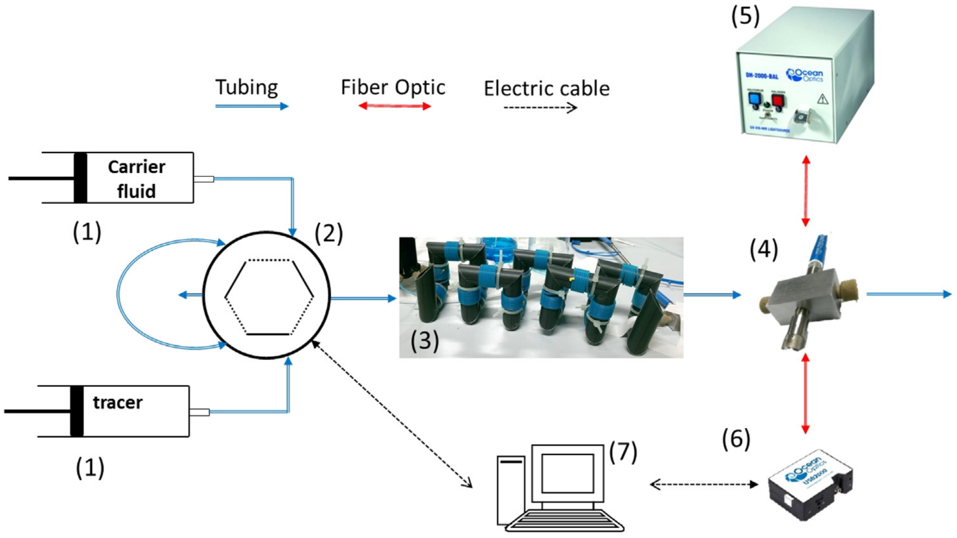

Fig. 2 – The experimental setup used for the RTD experiments consisted of a (1) syringe pump, (2) injection valve, (3) CFI, (4) non-intrusive flow cell, (5) source light, (6) spectrophotometer and (7) computer for data acquisition.

judge the quality of the fitting. The error ε is calculated as follows:

$$\varepsilon = \sum_i \left[E_{t,ADM}\left(D_{ax}, t_i\right) - E_{t,exp}\left(t_i\right)\right]^2 \tag{2.10}$$

where $E_{t,ADM}(D_{ax}, t_i)$ is the value of the analytical RTD curve at any time t_i and $E_{t,exp}(t_i)$ is the corresponding value of the experimental RTD curve.

We used this parameter to propose a criterion for the applicability of the ADM in systems other than straight channels (see Section 4.2), for which flow maps, such as that reported in Fig. 1, are unavailable.

3. Experimental procedure

3.1. *Experimental setup*

The experimental setup is pictured in Fig. 2. 25 ml SGE glass syringes were filled with carrier fluid (deionized water) and tracer fluid (aqueous solution of Basic Blue 3, Dye content 25%, Sigma-Aldrich). With a syringe pump (Harvard Apparatus PHD 2000), the fluids were simultaneously pumped to a six-way injection HPLC valve that allows switching between the tracer and the carrier fluid flowing within the channel; one fluid was disposed of as waste, while the other was fed to the millichannel. Initially the carrier fluid flowed through the channel; at a time t_0, the feed was abruptly switched to tracer fluid, generating a step in tracer concentration. At the channel outlet, optical fibers, connected to a light source (Ocean Optics DH-2000-BAL), shone light through the channel (PTFE capillary), which passed through a flow cell. The light that passed through the fluid reached, via optical fibers, a spectrophotometer (Ocean Optics USB2000 + UV–vis-ES) whereby the light intensity was measured at small regular time intervals. As discussed in more detail in the following section, prior to RTD measurements, light absorption by the tube wall and pure water was measured and removed as background signal.

3.2. *Effluent tracer and RTD measurement*

The tracer concentration was measured at the channel outlet to determine the RTD. To do so, the Lambert–Beer law (Eq. (3.1)) was used. This is a linear equation, valid at low tracer concentrations, that relates concentration to light absorption. Tests were conducted at different tracer concentrations to check the validity of the law. PTFE capillaries with OD 1.6 mm and ID 0.5, 0.8 and 1.0 mm were used for calibration. The absorbance was measured in stagnant conditions and three readings were taken. A deviation from linearity was observed at tracer concentrations greater than 200 mg/l. We therefore set the tracer concentration at the channel inlet equal to 100 mg/l.

The Lambert–Beer law is valid only when light travels perpendicularly to the flow direction (Parnis and Oldham, 2013), and reads:

$$A \equiv -\log\left(\frac{I}{I_0}\right) = \varphi l C \tag{3.1}$$

where I is the intensity of the light detected by the receiving sensor and I_0 is the intensity of the light emitted, φ is the extinction coefficient (a property of the medium), l is the path length of the beam of light through the material sample and C is the concentration of the tracer. The absorbance A was found as described below.

The flow cell is made of a rectangular aluminum block with four holes, one at the center of each lateral side. Two of them allow fitting the channel passing through the cell, while the other two accommodate the optical fibers. With this configuration the channel and the optical fibers are perpendicularly aligned to each other. The light beam leaving the channel via the optical fiber reached the spectrophotometer that measured its mean intensity. The light intensity depended entirely on the tracer concentration of the fluid present at the reactor outlet, because the carrier fluid and the tracer absorb light at different wavelengths. For this experiment the light intensity was averaged for wavelengths between 645 and 660 nm. The mean intensity measurements in the spectrophotometer were converted into absorbance values by using Eq. (3.1). For $t < t_0$, carrier fluid occupied the channel; this intensity value was taken and used as reference value. In Eq. (3.1), this value is I_0. For $t > t_0$, the light intensity I was measured. If the tracer concentration in the fluid that passes through the reactor outlet were zero, the intensity measurement would be approximately equal to I_0, the absorbance vanishing. For nonzero tracer concentrations, the light intensity decreases due to

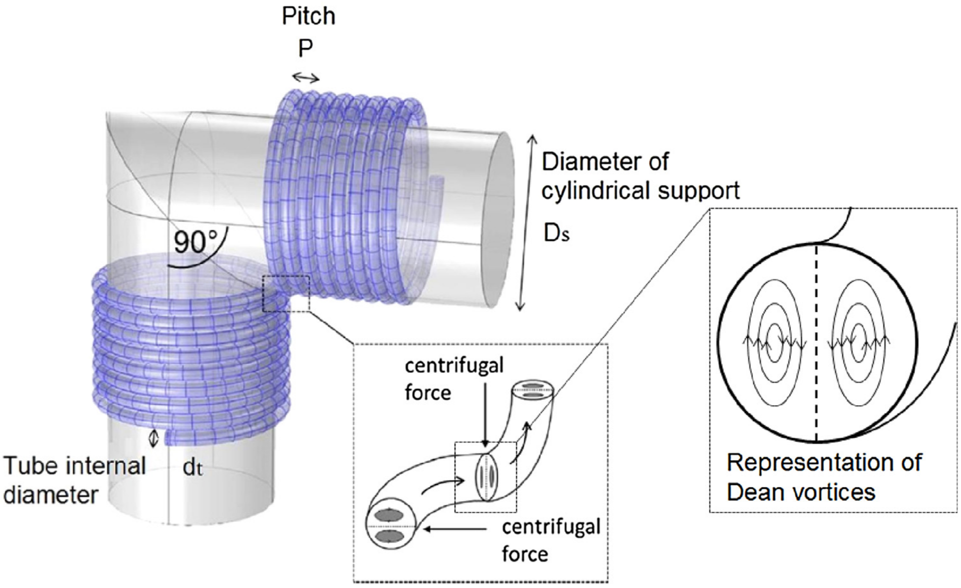

Fig. 3 – Schematic of a 90-degree bend in a CFI. In each helical coil section $n_a = 8$.

absorption at the 645–660 nm wavelengths, thus increasing the absorbance. Intensity measurements were taken at very small time intervals, thus enabling the absorbance to be plotted against time. Measurements were recorded using the Ocean Optics Spectra Suite software.

A MATLAB script was used to smooth the collected tracer concentration data $C(t)$ and reduce the noise arising from the measurements. The transformation of the experimental concentration curve $C(t)$ to the cumulative distribution function $F(t)$ was then achieved by normalizing the tracer concentration over the time:

$$F(t) = \frac{C(t)}{C_{max}} \tag{3.2}$$

Another MATLAB script was developed to differentiate the data from the first script. The RTD curve was thus produced. Differentiating Eq. (3.2) gives the experimental RTD curve:

$$E(t) = \frac{dF(t)}{dt} \tag{3.3}$$

3.3. *Design of HCTs and CFIs*

CFIs and HCTs were constructed using PVC tubes as supporting frame. For HCTs the support was a straight section of PVC pipe, while for CFIs the PVC pipe was cut in small sections with 45-degree edges and glued together forming a tridimensional frame. PTFE capillaries with different internal diameters were coiled on the PVC frame. A schematic representation of a 90-degree bend in a CFI is shown in Fig. 3.

The capillary was firmly secured on the supporting frame using cable ties. The axial pitch was minimized by having successive turns (tube coils or tube rings) contiguous so that the distance between successive turns equals the external diameter of the capillary.

Before presenting the design of the HCTs and CFIs employed in this work, the following dimensionless numbers need to be introduced.

- *Coil-to-tube diameter ratio*, λ. This number is related to the effect of centrifugal force on the flow and is defined as follows:

$$\lambda \equiv \frac{D_s}{d_t} \tag{3.4}$$

where D_s is the diameter of the cylindrical support and d_t is the internal diameter of the coiled tube. The inverse of the radius of a circle represents the curvature of the latter; thus, λ represents the ratio between the curvature of the coiled tube and that of the cylindrical support. Decreasing the value of λ results in a stronger centrifugal force; this is consequence of the increased curvature of the cylindrical support in relation to that of the coiled tube. The coil-to-tube diameter ratio is a crucial design parameter; however, its effect on the fluid dynamic behavior of CFIs has not been extensively investigated in the literature.

- *Dean number* ($De \equiv Re\lambda^{-0.5}$). This number relates to the balance between inertial, centrifugal and viscous forces. As De becomes small (i.e., less than unity), viscous forces become dominant and the effect of the centrifugal force vanishes. There exists a critical value of De (or of Re for any fixed value of λ) above which the effect of secondary flow enhances the reduction of axial dispersion. In the literature, it is suggested that the minimum value of De required to significantly flatten the velocity profile of a fluid is 3 (Klutz et al., 2015).

Our focus in this work was on the effect of the parameter λ rather than of the number of flow inversions, which has already been investigated in the literature. Moreover, data in the literature show that the number of bends n_b strongly affects axial dispersion (Saxena and Nigam, 1984). However, for $n_b < 7$ the difference with the RTD of a straight helix is minor. To effectively reduce axial dispersion Saxena and Nigam (1984) found that coiled flow inverters should be constructed keeping constant the number of turns on each arm, n_a. To investigate the effect of the curvature ratio alone, the number of bends n_b and the total number of turns n were kept constant for all CFIs constructed; in particular, we set $n_b = 19$ and $n = 160$. The value of n led to very long capillaries ranging between 9 and 19 m, depending on the diameter D_s of the particular CFI frame (Table 1). It was found by Saxena and Nigam (1984) $n_a = n/(n_b + 1) = 8$ to be the optimal number of turns on each arm of the CFIs (in their article, Saxena and Negam used

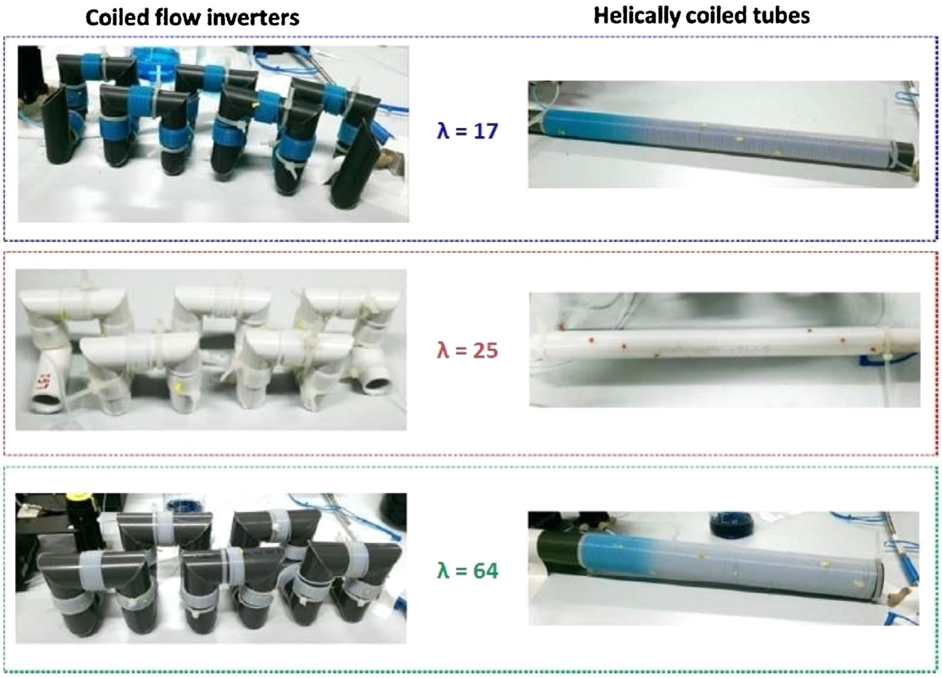

Fig. 4 – CFIs and HCTs constructed.

Table 1 – Geometrical parameters of the CFIs investigated.

λ	Coil-to-tube diameter ratio	17	25	64
D_s	Diameter of support [mm]	17	20	32
d_t	Internal diameter of tube [mm]	1.0	0.8	0.5
L	Length of tube [m]	9.75	11.25	18.85
p	Axial pitch [mm]	1.6	1.6	1.6
n_b	Number of bends	19	19	19
n_a	Number of turns on each arm	8	8	8
n	Total number of turns	160	160	160

the parameter $R_a = 1/(n_b + 1)$, which is different from n_a but related to it, being $R_a = n_a/n$). This value allowed the secondary flow to fully develop. To have sharp flow inversions, the free space on each arm of the CFI had to be minimized.

By changing both D_s and d_t, we could construct CFIs and HCTs with λ ranging between 17 and 64. The CFIs and HCTs constructed and investigated are shown in Fig. 4.

The inlet of the CFIs or HCTs was directly connected to the HPLC valve, so as to achieve a sharp step input directly at the inlet boundary. Their outlet was directly connected to the flow through cell (Fig. 2).

4. Results and discussion

4.1. *Determination of the molecular diffusion coefficient of the tracer*

In this section, we report how we determined the molecular diffusion coefficient D_m of the tracer in the carrier fluid employed. The exact value of D_m for Basic Blue 3 is not clearly known, as only a range of values for D_m is available in the literature (McKay et al., 1981).

As discussed in Section 2.1, when Bo is greater than 100, the molecular diffusion coefficient D_m in Eq. (2.6) can be neglected and so Eq. (2.6) reduces to Eq. (2.7), which can be rearranged as:

$$D_m = \frac{u^2 {d_t}^2}{192 D_{ax}} \tag{4.1}$$

This equation can be used to determine the value of the molecular diffusion coefficient from RTD experiments in straight tubes according to the following procedure:

- RTDs were measured in a straight capillary with aspect ratio $L/d_t = 5000$ under different values of the Reynolds number ($Re \equiv \rho u d_t/\mu$) by varying the fluid flow rate from 0.025 to 1 ml/min. According to Eq. (2.5), $Bo \equiv Re{\cdot}Sc$; therefore, when changing Re, the point representing the fluid dynamic condition of our system in the flow map regime of Fig. 1 follows a vertical line.
- The RTD curves measured experimentally were fitted with the analytical solutions of the ADM (Eqs. (2.8) and (2.9)). D_{ax} was the fitting parameter; thus D_{ax} was calculated from the experimental results. Fig. 5 shows sample fitted curves.
- The values of the molecular diffusion D_m were calculated using Eq. (4.1) and plotted against Re. The results are reported in Fig. 6.

We observed that when Re was smaller than about 2 the calculated molecular diffusivity D_m was constant (Fig. 6), being equal to 6.4×10^{-10} m^2/s, while for larger values of Re it increased with the latter. The increase does not have any physical basis: being an intrinsic transport property of the water-tracer system, D_m is not a function of Re. We concluded that the correct value of D_m was 6.4×10^{-10} m^2/s. This value lies within the measured range of values (3.78×10^{-10}–6.63×10^{-10} m^2/s) of the molecular diffusivity of Basic Blue 3 in water available in the literature (McKay et al., 1981).

Once the correct value of the coefficient of molecular diffusion was established, we could calculate the Bodenstein numbers for the experiments carried out and plot the oper-

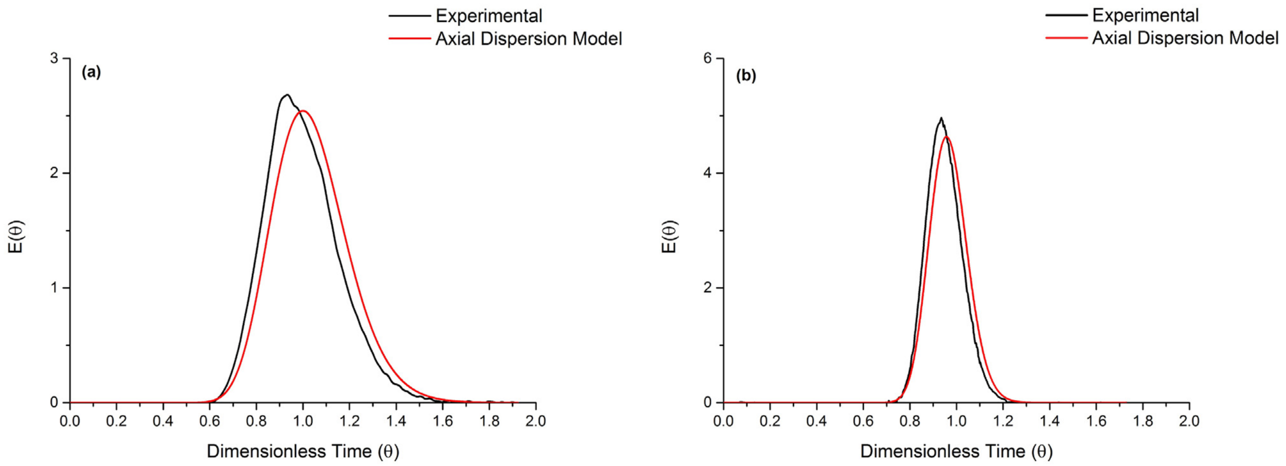

Fig. 5 – Sample E-curve fitting results for (a) Re = 21; D_m = 1.80 x 10^{-9} m^2/s; N_L = 0.0123. (b) Re = 1.58; D_m = 6.40 x 10^{-10} m^2/s; N_L = 0.0026.

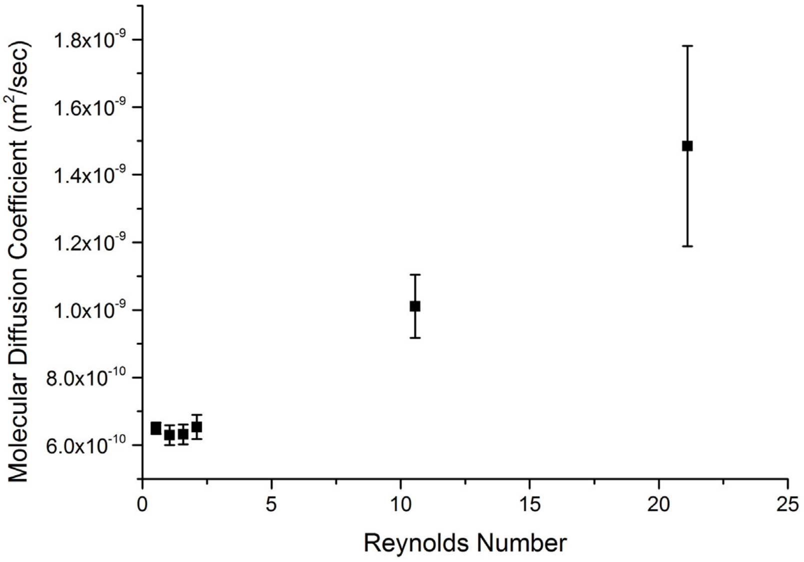

Fig. 6 – Calculated diffusion coefficient of Basic Blue 3 in water as a function of Re. Each experiment was performed three times and then the error bars shown were determined. For Re = 0.5, the error is ±1.7 x 10^{-11} m^2/s; the error bar is not visible.

ating points on the flow regime map (refer to Fig. 7). It can be observed that the experimental operating point obtained at the lowest flow rate of 0.025 ml/min ($Re = 0.5$) is positioned in the middle of the region of full applicability of the ADM. Here Bo = $8.29 \times 10^2 > 100$ and so Eq. (4.1) is valid. When the flow rate is increased, the operating point moves on the vertical line $L/d_t = 5000$ to higher values of the Bodenstein number. At flow rates larger than 0.1 ml/min, which corresponds to $Re = 2$ and Bo = 3.32×10^3, the coefficient of molecular diffusion is no longer constant and becomes a function of the Reynolds number. This value of Re also identifies the threshold in Fig. 6 after which the coefficient of molecular diffusion is no longer constant. The incorrect values of D_m obtained for Reynolds numbers above this threshold value arise because the operating point is close to the line separating the intermediate region from the zone of applicability of the ADM, so that Eq. (4.1) no longer holds.

Fig. 5a shows the dimensionless RTD curves for Re = 21.1. By definition, $E(\theta) \equiv \tau E(t)$, $\theta \equiv t/\tau$ and $\tau \equiv L/u$, where L is the length of the tube and u is the mean fluid velocity (Levenspiel, 1999).

For Re = 21.1, the system operates at the limit of applicability of ADM (see Fig. 7) and the highest error between experiments and model is observed. According to Levenspiel (1999), the width and the height of the RTD curve are strong functions of the vessel dispersion number. In Fig. 5a, the width and the height of the fitted and experimental curves are close, and the shapes of the curves are very similar; the fit is therefore good, and we conclude that Eqs. (2.8) and (2.9) can be deemed to be applicable. Fig. 5b shows that for a lower value of the Reynolds number (Re = 1.58), the ADM fits the experimental data very closely; thus, as expected, the ADM (that is, Eqs. (2.8) and (2.9)) applies.

4.2. *Criterion for applicability of the axial dispersion model in non-straight tubes*

In this section we introduce a general criterion for judging whether the ADM is applicable or not in geometries different than straight pipes.

As discussed in the previous section, to use Eq. (4.1), one must perform experiments under full applicability of the dispersion model, the validity of which depends on the value of Bo. The ADM developed by Taylor and Aris is derived for straight pipes, and therefore it might be invalid for other channel geometries. In this regard, a procedure to gather information on the applicability of the axial dispersion model is described below.

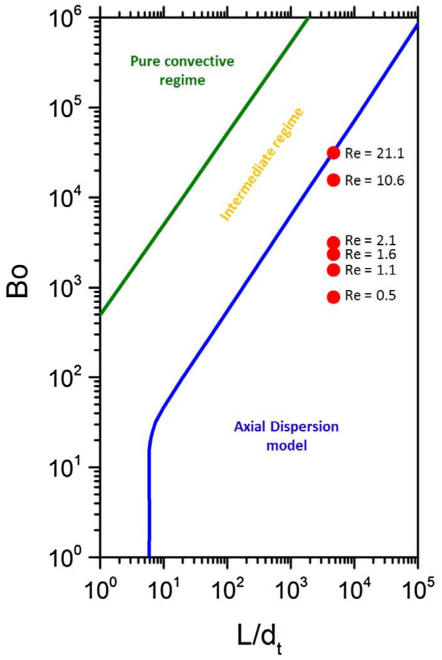

Fig. 7 – Operating points on the flow regime map. Range of applicability of the ADM.

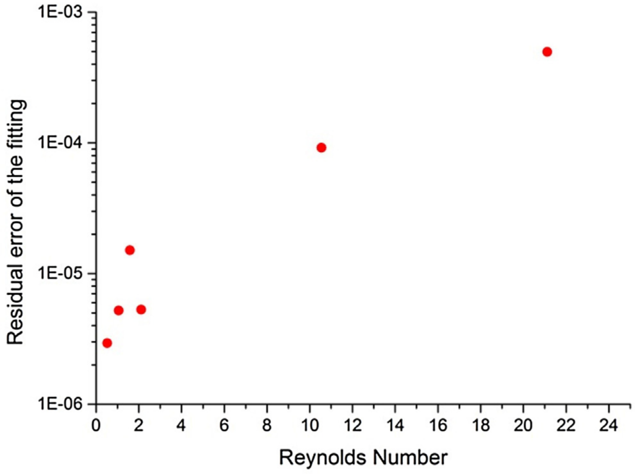

Fig. 8 – Residual error of the fitting of RTD experiments in a straight capillary with solutions of the ADM as a function of Re. Analytical solution of the ADM used: Eq. (2.8) for $N_L < 0.01$; Eq. (2.9) for $N_L > 0.01$. The fitting is based on the least squares method and is carried out using both equations and then, based on the value of the solutions, selecting the correct one.

We calculated the fitting errors ε at the different flow rates employed (0.025–1 ml/min) and we reported the values of ε as a function of the Reynolds number investigated (Fig. 8). From the plot, one can clearly observe that the residual error increases with *Re*. This is because an increase in *Re* leads to an increase in *Bo* (see Fig. 7). At high values of Bo, the system operates near the limit of applicability of ADM. As a result, the error ε increases while the system approaches this limit.

The experiments close to the boundary with the intermediate regime ($Re = 21.1$) generate the greatest error, while the residual error, and in turn the quality of the fitting, improves as *Re* decreases. For this reason, we identified $\varepsilon_{cr} = 10^{-3}$ as the critical value of the residual error that one should use in judging the applicability of the model. If residual error is beyond that limit, axial dispersion model is deemed to be invalid.

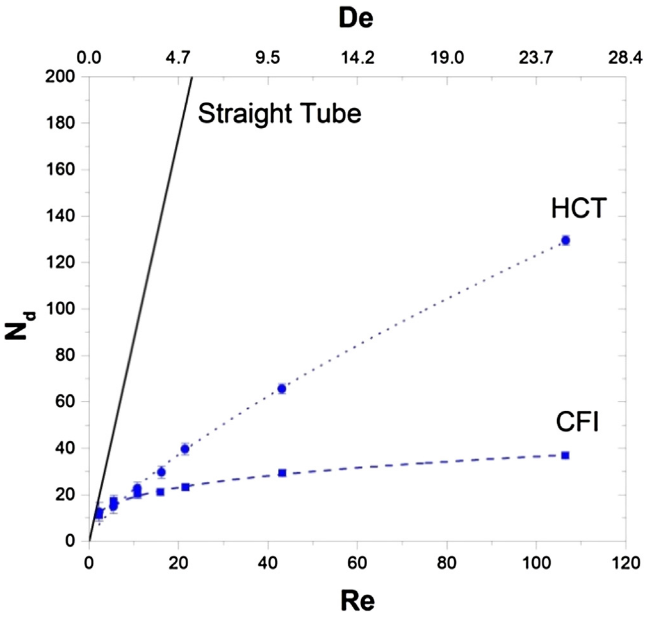

Fig. 9 – Axial dispersion number as a function of Re (primary axis) and De (secondary axis) for a CFI (squares) and a HCT (circles) for $\lambda = 17$. The straight line refers to Eq. (4.3). Maximum standard deviation of N_d is ±2.51. Not all error bars are visible.

4.3. *Axial dispersion in HCTs and CFIs*

The adoption of the dispersion number *Nd* is convenient because it allows comparing the extent of dispersion measured in CFIs and HCTs with that in straight tubes predicted by the Taylor–Aris equation for dispersion, Eq. (2.6). Written in terms of dispersion number, the equation becomes:

$$N_{d,TA} = \frac{1}{ReSc} + \frac{ReSc}{192} \tag{4.2}$$

The first term on the right hand side of Eq. (4.2) can be neglected, because it is significant only for $Bo < 100$ and in this work the Bodenstein number ranged between 10^4 and 10^5. Also, the Schmidt number was kept constant as deionized water and aqueous solutions of Basic Blue 3 were used as carrier fluid and tracer, respectively. The properties of the fluid were assumed to be those of water at room temperature ($\rho = 997\,\mathrm{kg/m^3}$, $\mu = 1.002 \times 10^{-3}\,\mathrm{Pa\,s}$) and the diffusion coefficient of the tracer in water, measured experimentally in a straight capillary (see Section 4.1) was $6.40 \times 10^{-10}\,\mathrm{m^2/s}$, leading to $Sc = 1677$. Eq. (4.2) can then be written as follows:

$$N_{d,TA} = (Sc/192)\,Re = 8.7Re \tag{4.3}$$

Eq. (4.3) expresses the relationship between dispersion and Reynolds numbers for straight pipes. $N_{d,TA}$ is an increasing linear function of *Re* for any given value of *Sc*.

The results of experiments on both CFIs and HCTs with different values of λ are reported in Figs. 9–11. The plots show the value of N_d as a function of *Re*. The different values of the Reynolds number are obtained by changing the flow rate between 0.05 ml/min and 5 ml/min. The corresponding values of the Dean number are calculated and displayed on a secondary axis. As a reference, the curve for straight tubes is

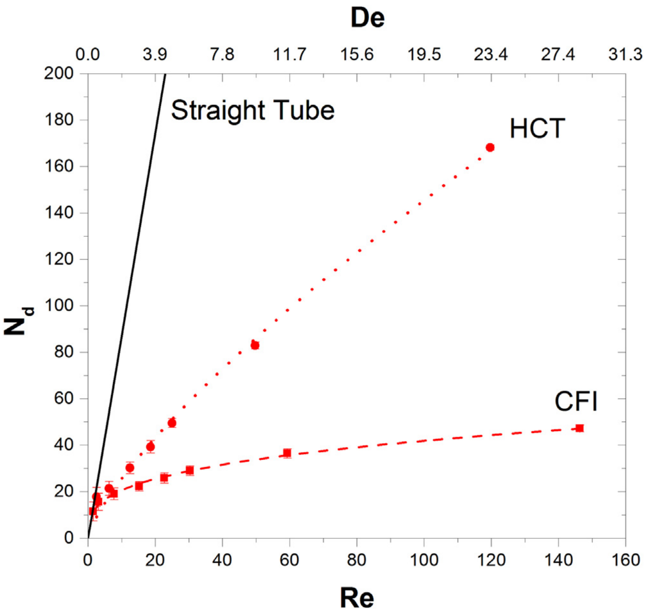

Fig. 10 – Axial dispersion number as a function of Re (primary axis) and De (secondary axis) for a CFI (squares) and a HCT (circles) for λ = 25. The straight line refers to Eq. (4.3). Maximum standard deviation of N_d is ±4.39. Not all error bars are visible.

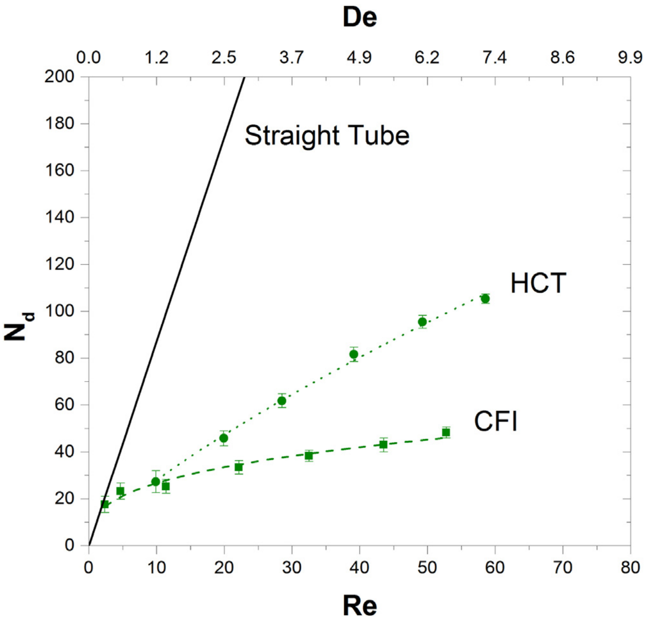

Fig. 11 – Axial dispersion number as a function of Re (primary axis) and De (secondary axis) for a CFI (squares) and a HCT (circles) for λ = 64. The straight line refers to Eq. (4.3). Maximum standard deviation of N_d is ±3.21. Not all error bars are visible.

also reported (Eq. (4.3)). The values of *Nd* were averaged over three experiments for each set of parameters. The standard deviation is shown as error bars on the data points.

For any value of the coil-to-tube diameter ratio, both HCTs and CFIs show less dispersion than straight tubes, confirming that the secondary flow plays a major role in defining the dispersion behavior. In CFIs the reduction of axial dispersion is as large as 10-fold for the higher values of the Reynolds number investigated. The dispersion number increases with the Reynolds number, but at a rate smaller than that of straight tubes. The rate appears to depend on Re, λ and the type of configuration. The curves for CFIs increase at a smaller rate than those for HCTs, suggesting that flow inversion has a strong effect on the dispersion behavior. It can also be observed that the rate decreases with *Re*, revealing a different trend as compared with straight tubes, for which the correlation is linear.

As *Re* tends to zero, the dispersion curves for HCTs and CFIs approach the line for straight pipes. This is expected because at low values of *Re* the intensity of secondary flow, quantified by *De*, is modest and the Dean roll-cells, which are primarily responsible for the reduction in dispersion, disappear. When *De* decreases the dispersion behavior of HCTs and CFIs meets the one obtained for straight tubes. This point can be roughly estimated by analyzing the curves reported: it appears that all data point with $De < 0.5$ approach closely the curve for straight tubes. It was suggested in the literature that when $De < 0.25$ one can use the Taylor–Aris dispersion equation to quantify the dispersion in HCTs (Erdogan and Chatwin, 1967; Nigam and Vasudeva, 1976). This agrees with our findings.

For any value of λ, CFIs are characterized by lower dispersion compared to HCTs; this confirms the observations of Saxena and Nigam (1984). They reported that significant reduction in axial dispersion was achieved compared to HCTs. Moreover, they observed that the vessel dispersion number ($NL = Dax/uL$) did not depend on *De*, for CFIs with $nb = 15, 30, 57$ in the range $2 < De < 60$. Our results are qualitatively different because *Nd* increases with *De*, meaning that as the secondary flow intensifies, so does the reduction on the dispersion behavior. Note that *Nd* and *NL* are qualitatively equivalent, as $NL = Nd \cdot (dt/L)$. The importance of flow inversion in creating further radial mixing and in narrowing down the RTD lies in the change of direction of the centrifugal force, which makes the position of the Dean roll-cells vary. In the absence of secondary flow (and so of Dean roll-cells) the effect of flow inversion is expected to vanish. For *De* less than about 2 the curves for HCTs and CFIs overlap before approaching the curve of the straight tubes. This suggests the existence of a narrow region ($0.5 < De < 2$) in which the centrifugal force still reduces axial dispersion, but the Dean roll-cells are not strong enough to induce chaotic mixing at the bends. As a result, when operating in this region, HCTs and CFIs behave identically in terms of axial dispersion.

4.4. *Effect of coil-to-tube diameter ratio*

The effect of the coil-to-tube diameter ratio was investigated in CFIs and is shown in Fig. 12. A significant dependence of *Nd* on λ can be observed in the range investigated. The dependence is stronger at larger values of *Re*. As the mean velocity increases (and so *Re*), the centrifugal force, also dependent on λ, that acts on the fluid intensifies. This results into stronger recirculation owing to Dean roll-cells and more effective flow inversion. Conversely, the coil-to-tube diameter ratio has a lower impact on the magnitude of axial dispersion in HCTs (Fig. 13). This can be explained considering that in CFIs two mechanisms contribute to the reduction of axial dispersion: Dean roll-cells in the sections of straight helical coils and change of orientation of Dean roll-cells at the bends. Consequently, for a given value of *Re*, when λ decreases, the stronger secondary flow manifests both in the straight helical coils and at the bends. The second mechanism is absent in HTCs; this explains the weaker dependence of the axial dispersion number on λ. These observations suggest that λ can be used more effectively in CFIs as a design parameter for narrowing down the RTD for a given value of *Re*.

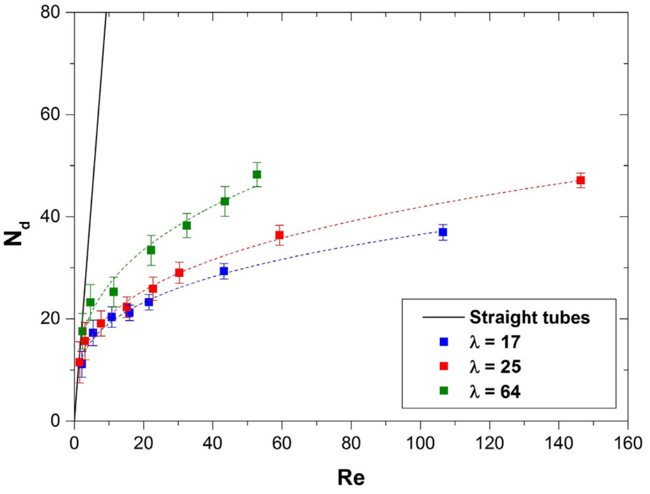

Fig. 12 – Axial dispersion number as a function of Re for CFIs at different λ. The straight line refers to Eq. (4.3).

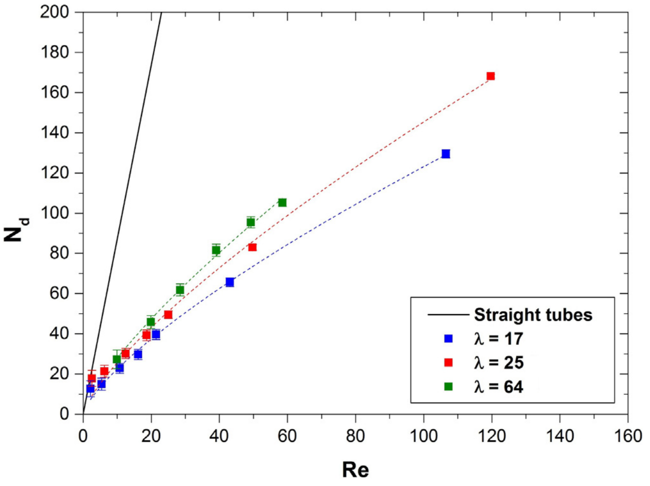

Fig. 13 – Axial dispersion number as a function of Re for HCTs at different λ. The straight line refers to Eq. (4.3).

The values of dispersion number obtained experimentally were correlated to the values of *Re* using a generalized version of the Taylor–Aris equation for dispersion:

$$N_d = (Sc/192)\,k_1(\lambda)\,Re^{k_2(\lambda)} \tag{4.4}$$

where the values of $k_1(\lambda)$ and $k_2(\lambda)$ are found with a least squares method. The fitted curves are reported as dashed-lines in Figs. 12 and 13. We assumed that k_1 and k_2 only depend on λ, as any other parameter was kept constant.

The choice of a power law is consistent with the curve trends. The values of k_1 and k_2 and the analytical expressions of the functions $k_1(\lambda)$ and $k_2(\lambda)$ are reported for both CFIs and HCTs in Table 2. It can be observed that the vessel dispersion number has a weaker dependence on the Reynolds number in CFIs compared to HCTs.

The proposed equation matches very well the data in the range investigated. It should be stressed that the values found are only valid for $n_b = 19$ and $n = 160$.

4.5. *Applicability of the axial dispersion model in CFIs and HCTs*

In this section, we investigated the applicability of the axial dispersion model for CFIs and HCTs. Fig. 14 shows the residual error of the ADM curves used to fit the experimental results as a function of the Reynolds number, for both structures. As discussed in Section 4.2 for straight tubes, the residual error ε increases with the Reynolds number, because the operating conditions of the system progressively move away from the region of full validity of the ADM (Fig. 7). A similar behavior is observed in Fig. 14. The criterion that we have proposed to judge the applicability of the ADM requires that the residual error should be lower than $\varepsilon_{cr} = 10^{-3}$. We considered only experiments fulfilling this criterion, as Fig. 14 confirms.

5. Conclusions

The main goal of this work was to investigate the dispersion characteristics of coiled flow inverters by conducting RTD experimental studies. A setup was developed to measure reliably RTDs in CFIs and, more in general, in different milli and microfluidic devices. Experiments in straight capillaries were also conducted to measure the molecular diffusion coefficient of the tracer in water and to generate a criterion for the applicability of the axial dispersion model in systems different than straight tubes.

Understanding the dependence of the principal geometrical parameters on the dispersion characteristic is crucial for the optimal design of CFIs. In this work, the effect of the coil-to-tube diameter ratio and of the Reynolds number was

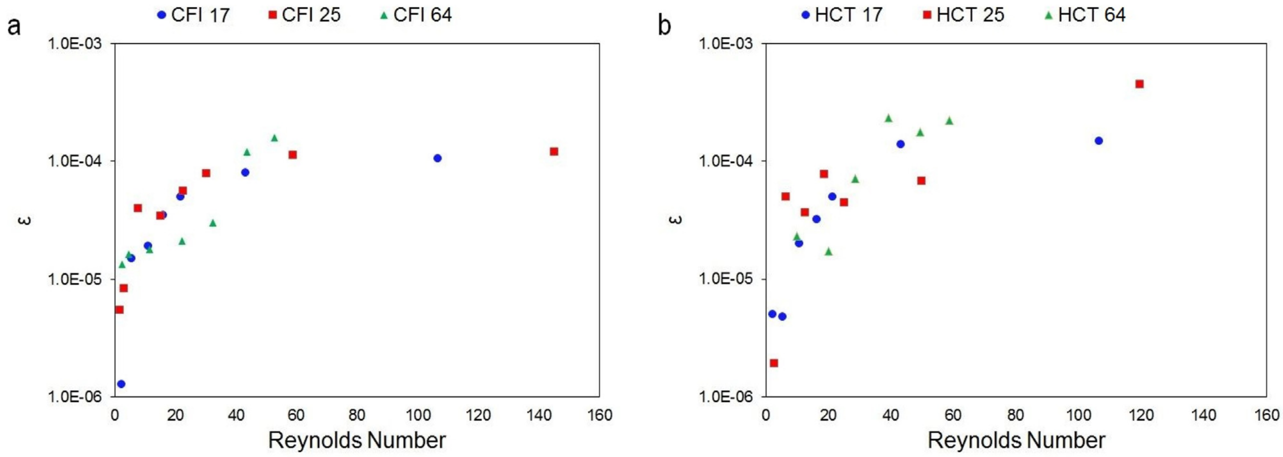

Fig. 14 – Residual error of the fitting of RTD experiments performed in (a) CFIs and (b) HCTs with the solutions of ADM as a function of Re.

Table 2 – Fixed values of k_1 and k_2 for both HCT and CFI.

Coil-to-tube diameter ratio	HCT		CFI	
	k_1	k_2	k_1	k_2
17	0.466	0.740	1.142	0.281
25	0.515	0.754	1.159	0.308
64	0.551	0.763	1.438	0.327
	$k_1 = 1.53 \times 10^{-3}\lambda + 0.46$		$k_1 = 6.57 \times 10^{-3}\lambda + 1.01$	
	$k_2 = 4.07 \times 10^{-4}\lambda + 0.74$		$k_2 = 8.22 \times 10^{-4}\lambda + 0.28$	

investigated in HCTs and CFIs constructed using capillaries (with ID up to 1.0 mm) and PVC pipes as supporting structures. The coil-to-tube diameter ratio was found to influence the intensity of dispersion more significantly in CFIs than in HCTs. This demonstrates that flow inversion is extremely effective at narrowing down the RTD. However, it was also observed that flow inversion is active only for values of the Dean number above two. The operating value of the Dean number can be tuned by varying the value of the Reynolds number and of the coil-to-tube diameter ratio. The value of the former is often dictated by the operating conditions (flow rate and fluid properties) of the process. For a given Reynolds number, the value of the coil-to-tube diameter ratio must be as small as possible.

For CFIs to be adopted on a larger scale, it would be useful to obtain correlations relating the dispersion number to design and operating parameters. In this work, it was found that the dispersion number correlates with the Reynolds number according to a power law. This was obtained for fixed values of the Schmidt number and of numbers of bends and turns.

Acknowledgment

The authors would like to thank EPSRC for funding (EP/I031480/1).

Appendix A. Supplementary data

Supplementary data associated with this article can be found, in the online version, at http://dx.doi.org/10.1016/j.cherd.2017.02.011.

References

Acharya, N., Sen, M., Hsueh-Chia, C., 1992. Heat transfer enhancement in coiled tubes by chaotic mixing. Int. J. Heat Mass Transf. 35 (10), 2475–2489.

Acharya, N., Sen, M., Chang, H.C., 2001. Analysis of heat transfer enhancement in coiled-tube heat exchangers. Int. J. Heat Mass Transf. 44 (17), 3189–3199.

Ananthakrishnan, V., Gill, W.N., Barduhn, A.J., 1965. Laminar dispersion in capillaries: part I. Mathematical analysis. AIChE J. 11, 1063–1072.

Aris, R., 1960. On the dispersion of a solute in pulsating flow through a tube. Proc. R. Soc. A: Math. Phys. Eng. Sci. 259 (1298), 370–376.

Castelain, C., et al., 1997. Residence time distribution in twisted pipe flows: helically coiled system and chaotic system. Exp. Fluids 22 (5), 359–368.

Chagny, C., Castelain, C., Peerhossaini, H., 2000. Chaotic heat transfer for heat exchanger design and comparison with a regular regime for a large range of Reynolds numbers. Appl. Therm. Eng. 20 (17), 1615–1648.

Danckwerts, P.V., 1953. Continuous flow systems. Chem. Eng. Sci. 2, 1–13.

Erdogan, M.E., Chatwin, P.C., 1967. The effects of curvature and buoyancy on the laminar dispersion of solute in a horizontal tube. J. Fluid Mech. 29, 465–484.

Hessel, V., Löwe, H., Schönfeld, F., 2005. Micromixers—a review on passive and active mixing principles. Chem. Eng. Sci. 60, 2479–2501.

Hohmann, L., et al., 2016. Design of a continuous tubular cooling crystallizer for process development on lab-scale. Chem. Eng. Technol. 39 (7), 1268–1280.

Kateja, N., et al., 2016. Continuous precipitation of process related impurities from clarified cell culture supernatant using a novel coiled flow inversion reactor (CFIR). Biotechnol. J. 11 (10), 1320–1331.

Klutz, S., et al., 2015. Narrow residence time distribution in tubular reactor concept for Reynolds number range of 10–100. Chem. Eng. Res. Des. 95, 22–33.

Klutz, S., et al., 2016. Continuous viral inactivation at low pH value in antibody manufacturing. Chem. Eng. Process.: Process Intensif. 102, 88–101.

Kumar, V., Nigam, K.D.P., 2005. Numerical simulation of steady flow fields in coiled flow inverter. Int. J. Heat Mass Transf. 48 (23–24), 4811–4828.

Kumar, V., Nigam, K.D.P., 2007. Laminar convective heat transfer in chaotic configuration. Int. J. Heat Mass Transf. 50 (13–14), 2469–2479.

Kurt, S.K., et al., 2016. Liquid–liquid extraction system with microstructured coiled flow inverter and other capillary setups for single-stage extraction applications. Chem. Eng. J. 284, 764–777.

Lemenand, T., Peerhossaini, H., 2002. A thermal model for prediction of the Nusselt number in a pipe with chaotic flow. Appl. Therm. Eng. 22 (15), 1717–1730.

Levenspiel, O., Smith, W.K., 1957. Notes on the diffusion-type model for the longitudinal mixing of fluids in flow. Chem. Eng. Sci. 6, 227–233.

Levenspiel, O., 1999. Chemical Reaction Engineering, 3rd ed. John Wiley & Sons, New York.

Mandal, M.M., Kumar, V., Nigam, K.D.P., 2010. Augmentation of heat transfer performance in coiled flow inverter vis-à-vis conventional heat exchanger. Chem. Eng. Sci. 65 (2), 999–1007.

Mandal, M.M., et al., 2011. Numerical modeling of polystyrene synthesis in coiled flow inverter. Microfluid. Nanofluid. 10 (2), 415–423.

Marre, S., Jensen, K.F., 2010. Synthesis of micro and nanostructures in microfluidic systems. Chem. Soc. Rev. 39 (March), 1183–1202.

McKay, Otterburn, M.S., Sweeney, A.G., 1981. Surface mass transfer processes during colour removal from effluent using silica. Water Res. 15, 327–331.

Mokrani, A., Castelain, C., Peerhossaini, H., 1997. The effects of chaotic advection on heat transfer. Int. J. Heat Mass Transf. 40 (13), 3089–3104.

Mridha, M., Nigam, K.D.P., 2008. Numerical study of turbulent forced convection in coiled flow inverter. Chem. Eng. Process.: Process Intensif. 47 (5), 893–905.

Nguyen, N.-T., Wu, Z., 2005. Micromixers—a review. J. Micromech. Microeng. 15 (February), R1–R16.

Nigam, 2008 is a patent (http://www.google.co.uk/patents/US7337835). It is a United States Patent. Patent N0.: US 7,337,835 B2.

Nigam, K.D.P., Vasudeva, K., 1976. Influence of curvature and pulsations on laminar dispersion. Chem. Eng. Sci. 31, 835–837.

Palazoglu, T.K., Sandeep, K.P., 2004. Effect of tube curvature ratio on the residence time distribution of multiple particles in helical tubes. LWT—Food Sci. Technol. 37 (4), 387–393.

Parida, D., et al., 2014a. Flow inversion: an effective means to scale-up controlled radical polymerization tubular microreactors. Macromol. React. Eng. 8 (8), 597–603.

Parida, D., et al., 2014b. Coil flow inversion as a route to control polymerization in microreactors. Macromolecules 47 (10), 3282–3287.

Parnis, J.M., Oldham, K.B., 2013. Beyond the Beer–Lambert law: the dependence of absorbance on time in photochemistry. J. Photochem. Photobiol. A: Chem. 267, 6–10.

Saxena, A.K., Nigam, K.D.P., 1984. Coiled configuration for flow inversion and its effect on residence time distribution. AIChE J. 30, 363–368.

Schaschke, C., 2014. A Dictionary of Chemical Engineering, second ed. OUP Oxford, Oxford.

Sharma, A.K., et al., 2016. Continuous refolding of a biotech therapeutic in a novel Coiled Flow Inverter Reactor. Chem. Eng. Sci. 140, 153–160.

Sharma, L., Nigam, K.D.P., Roy, S., 2017. Single phase mixing in coiled tubes and coiled flow inverters in different flow regimes. Chem. Eng. Sci. 160, 227–235.

Singh, J., Choudhary, N., Nigam, K.P., 2014. The thermal and transport characteristics of nanofluids in a novel three-dimensional device. Can. J. Chem. Eng. 92 (12), 2185–2201.

Singh, J., Srivastava, V., Nigam, K.D.P., 2016. Novel membrane module for permeate flux augmentation and process intensification. Ind. Eng. Chem. Res. 55 (13), 3861–3870.

Squires, T.M., Quake, S.R., 2005. Microfluidics fluid physics at the nanoliter. Rev. Mod. Phys. 77, 977–1026.

Taylor, G., 1953. Dispersion of soluble matter in solvent flowing slowly through a tube. Proc. R. Soc. A: Math. Phys. Eng. Sci. 219, 186–203.

Taylor, G.I., 1961. Deposition of a viscous fluid on a plane surface. J. Fluid Mech. 9, 218.

Vashisth, S., Nigam, K.D.P., 2007. Experimental investigation of pressure drop during two-phase flow in a coiled flow inverter. Ind. Eng. Chem. Res. 46 (14), 5043–5050.

Vashisth, S., Nigam, K.D.P., 2008a. Experimental investigation of void fraction and flow patterns in coiled flow inverter. Chem. Eng. Process.: Process Intensif. 47 (8), 1287–1297.

Vashisth, S., Nigam, K.D.P., 2008b. Liquid-phase residence time distribution for two-phase flow in coiled flow inverter. Ind. Eng. Chem. Res. 47 (10), 3630–3638.

Vashisth, S., Kumar, V., Nigam, K.D.P., 2008. A review on the potential applications of curved geometries in process industry. Ind. Eng. Chem. Res. 47 (10), 3291–3337.

Vural Gürsel, I., et al., 2016. Utilization of milli-scale coiled flow inverter in combination with phase separator for continuous flow liquid–liquid extraction processes. Chem. Eng. J. 283, 855–868.

Zhang, L., et al., 2017. Co and Ni extraction and separation in segmented micro-flow using a coiled flow inverter. Chem. Eng. J. 307, 1–8.